

An Indo-Pacific see-saw wobbles the Earth at intraseasonal timescales

M Afroosa

Indian National Centre for Ocean Information Services

B Rohith

Indian National Centre for Ocean Information Services (INCOIS) <https://orcid.org/0000-0003-3187-0781>

Arya Paul (✉ aryapaul@incois.gov.in)

Indian National Centre for Ocean Information Services <https://orcid.org/0000-0002-6635-3058>

Fabien Durand

LEGOS, Université de Toulouse, IRD, CNRS, CNES, UPS

Romain Bourdallé-Badie

Mercator Ocean International

P.V. Sreedevi

Indian National Centre for Ocean Information Services

Olivier de Viron

U. La Rochelle

Valérie Ballu

Laboratoire Littoral Environnement et Socié <https://orcid.org/0000-0002-7985-4636>

S.S.C. Shenoi

Indian National Centre for Ocean Information Services

Article

Keywords: Barotropic Response, Madden-Julian Oscillation, Ocean General Circulation Model

Posted Date: October 29th, 2020

DOI: <https://doi.org/10.21203/rs.3.rs-88417/v1>

License:  This work is licensed under a Creative Commons Attribution 4.0 International License.

[Read Full License](#)

Version of Record: A version of this preprint was published at Communications Earth & Environment on July 5th, 2021. See the published version at <https://doi.org/10.1038/s43247-021-00210-x>.

Abstract

Strong large-scale winds can relay their energy to the ocean bottom and elicit an almost immediate intraseasonal barotropic (depth independent) response in the ocean. The intense winds associated with the Madden-Julian Oscillation (MJO), over the tropical interface between the Indian Ocean and the Pacific Ocean (popularly known as Maritime Continent) generate significant basin-wide intraseasonal barotropic sea level variability in the tropical Indian Ocean. Here we show, using an ocean general circulation model and a network of in-situ bottom pressure recorders, that the concerted barotropic response of the Indian and the Pacific Ocean to these winds leads to an intraseasonal see-saw of oceanic mass in the Indo-Pacific basin. This global-scale mass shift is unexpectedly fast, as we show that the mass field of the entire Indo-Pacific basin is dynamically adjusted to MJO in a few days. We also explain how this near-global-scale MJO-induced oceanic phenomenon is the first signature from a climate mode that can be isolated into the Earth polar axis motion, in particular during the strong see-saw of early 2013.

Main Text

The Madden-Julian Oscillation (MJO) is the most energetic large-scale intraseasonal atmospheric disturbance^{1,2}. It originates in tropical Africa, travels eastward towards Indian and Pacific basins and returns to Africa every 30-80 days. Strong boreal winter MJO is associated with intense winds over the Maritime Continent, the tropical interface between the Indian and the Pacific Ocean, generating significant intraseasonal barotropic sea level variability in the entire tropical Indian Ocean (TIO)³. It amounts to a basin-scale signal of 4-6 cm in the entire TIO, with the mass redistribution achieved through fast-propagating barotropic waves adjusting the TIO in ~2-3 days³. We report that during boreal winter MJO, the rise of oceanic mass in the TIO is concurrent with a fall of oceanic mass in the Pacific Ocean, and vice-versa at intraseasonal timescales. The periodic reversal of MJO winds therefore leads to an intraseasonal see-saw in the oceanic mass in the Indo-Pacific basin, with the fulcrum stationed over the Maritime Continent. Due to the extent of Pacific Ocean – well beyond the tropics – this fast barotropic dynamics incites a far-reaching, quasi-global oceanic response to the MJO encompassing tens of thousands of kilometers within a few days. This discovery challenges the earlier understanding of a response only via slow-propagating baroclinic waves thereby adjusting the density field of the basins in ~2-3 months^{4,5}.

The see-saw generation involves large-scale mass redistribution and currents across and within the Pacific and Indian basins. The associated global-scale angular momentum, coming both from a near-global rotation of the ocean or a global-scale mass redistribution, is expected to leave its signature in the Earth's rotation^{6,7}. The Earth's rotation is not constant, and presents fluctuations in a broad range of frequencies^{8,9}. Most of those signals come from the variability in the angular momentum of the Earth's core and the atmosphere⁸. The signature from the ocean is more elusive, because the geometry of the ocean, interspersed with continental landmasses, is not optimal to generate a strong global angular momentum fluctuation associated with an observable impact on the Earth's rotation. The polar motion,

i.e. the wobble of the solid Earth around its rotation axis, has an even less favorable geometry: it can be excited by either a global current corresponding to a rotation around an axis at the equator or a global-scale mass anomaly with a 45°-tilted ellipsoid¹⁰. An ocean impact over polar motion can thus only be generated by strong global-scale dynamics, with a very particular geometry. As a consequence, though the ocean is believed to be a major driver of the polar motion, there is hitherto only little evidence of climate modes excitation of the polar motion through the ocean. Nevertheless, our study demonstrates that the MJO-induced see-saw, being a near-global process, does leave oceanic footprints on the polar motion.

Revelation of the see-saw. The see-saw is evidenced through a high-resolution global ocean circulation model, Nucleus for European Modelling of the Ocean (NEMO)¹¹, which can resolve adequately the narrow Indonesian straits between the Indian and Pacific basins. The control run (Methods) covers the 2009-2019 period and captures fairly well the Indonesian Throughflow (ITF) transports (Supplementary Fig.S1) and the observed ocean mass variability at intraseasonal timescales (Supplementary Fig.S2). This whole study focuses on intraseasonal timescales (30-80 days band) during boreal winter (December-April) months. We define a See-saw Index as the normalized difference of mean Equivalent Water Depth Anomaly (EWDA) from the control run between two equatorial boxes ((65°E:75°E, 5°S:5°N) and (155°W:165°W, 5°S:5°N)) in the Indian and Pacific Ocean. A positive index indicates a high water level in the Indian Ocean and a low water level in the Pacific Ocean. In Fig.1a, the time-series of the See-saw Index (shaded grey) and the net volume flux into the Indian (red line) and the Pacific (blue line) Ocean are plotted for the period 2009-2019. The See-saw Index variability is strongest during 2011-12 and 2012-13 - two winters of strong MJO activity (Fig.1c) over the Maritime Continent. Most of the time, and in particular during intense MJO events, the two volume fluxes are in opposition of phase, i.e., a net inflow of water in the Indian Ocean is accompanied by a net outflow of water from the Pacific Ocean and vice versa, thereby displaying characteristics of a see-saw in the Indo-Pacific basin. As expected, the maximum transports occur at the times of sign change of the See-saw Index (Fig.1b). During a strong positive (negative) See-saw Index peak, ~1.5 Sv (2.6 Sv) [1 Sv = $10^6 \text{ m}^3 \text{s}^{-1}$] of water is gained (lost) in the Indian (Pacific) Ocean, which is equivalent to a spatially uniform basin rise (fall) of ~1.0 cm (0.8 cm) of EWD in the Indian (Pacific) Ocean (Supplementary Fig.S3).

To explore the spatial extent of this see-saw, the EWDA over the Maritime Continent (at the location of the yellow star on Fig.2a) is correlated with the EWDA at all model grid locations during December-April. Interestingly, a basin-wide rise in EWD in the TIO is accompanied by a large-scale fall in EWD extending over the tropics, the southern extratropics and the northern edge of the Pacific Ocean and over most parts of the Arctic Ocean (Fig.2a). In contrast, only isolated small patches in the Atlantic Ocean participate in this coherent dance of oceanic mass. It is striking to discover that a large-scale see-saw of oceanic mass encompasses the vast majority of the world ocean.

Role of MJO. The large-scale EWDA variability in TIO is driven by MJO winds over the Maritime Continent³. To determine to which extent the MJO winds also drive the large-scale variability in the Pacific

Ocean, a sensitivity model experiment (MC-EXP; Methods) is run for the 2009-2019 period, with wind forcing restricted to the Maritime Continent (black box in Fig.2b). The spatial correlation of EWDA over the Maritime Continent from MC-EXP during each December-April with the same at all model grid points is plotted in Fig.2b. The correlation pattern in the Indo-Pacific basin is, to a large extent, similar to the correlation pattern obtained from the control run (Fig.2a). So, the intraseasonal see-saw in the Indo-Pacific basin persists even if the model is forced only by winds over the Maritime Continent. Note that the signature is not consistent with what is observed in the EWDA in the Arctic and North Pacific Ocean, most probably due to dominant local dynamics^{13,14}.

Whereas the MC-EXP largely captures the variance in the TIO (with values >70%)³, its impact is also significant over the Pacific Ocean (Fig.2c). The winds over the Maritime Continent alone can generate as much as ~30% of the variance in EWDA over the tropical and southern Pacific Ocean. It is remarkable that the wind forcing from such a small region (~4% of global ocean coverage) casts such a large-scale influence and excites ~15-30% of the intraseasonal oceanic mass fluctuations over a large part of the tropical Pacific.

During a positive cycle of the index, the MJO winds drive ~2 Sv of Pacific waters into the Indian Ocean through the ITF. An equivalent flux is subsequently flushed out into the Southern Ocean after ~1-2 days. The Southern Ocean conveys it eastward and subsequently injects ~2 Sv into the Pacific Ocean after another ~1 day, thereby closing this anti-clockwise circulation around the Australian continent (Supplementary Fig.S4). This barotropic circulation is schematically illustrated in Fig.2d. As expected, the circulation reverses its direction during the negative phase of the see-saw. This intraseasonal circulation occurs over and above a permanent anti-clockwise barotropic circulation around the Australian continent¹⁵. It is this intraseasonal reversing circulation that drives the Indo-Pacific see-saw.

Observational imprint of the see-saw. We investigated the imprint of the intraseasonal see-saw through the Bottom Pressure Recorder (BPR) network, although this network is very sparse. Fig.3a shows the evolution of intraseasonal EWDA from two BPRs, one located in the Maritime Continent (BPR-MC; red line) and another one in the central Pacific Ocean (BPR-PAC; blue line) during boreal winters of 2009-2019 (see Methods for data processing). BPR-PAC is often out-of-phase with BPR-MC, particularly in 2011-12 and 2012-13 when the MJO wind stress was strong over the Maritime Continent. The variability in the Indian Ocean amounts to 4-6 cm peak-to-peak, that of the Pacific Ocean is ~2-3 cm - half compared to the Indian Ocean. EWDA at BPR-MC was correlated with EWDA from all available BPRs globally (Fig.3b). All the Indian Ocean BPRs synchronously oscillate, whereas many of the Pacific BPRs (~42% of all analyzed Pacific BPRs) and all BPRs in the Arctic Ocean are anti-correlated with the Indian Ocean BPRs. The observed features are in line with the model results, and consistent with what is expected from the existence of a large-scale see-saw between the Indian and the Pacific basins.

See-saw impact on polar motions.

The geometry of the see-saw circulation (Fig.2d) is near optimal for generating a large signature in the polar motion excitation. In addition, the North-South asymmetry of the global-scale mass distribution anomaly also impacts the polar motion. The excitation of the polar motion is classically estimated using excitation functions – χ_1 for rotation around an axis at the Greenwich meridian (x-axis) and χ_2 for rotation around an axis that passes through the Indian Ocean at 90°E (y-axis) – representing the amount of additional rotation provided by the ocean (Methods). Considering the geometry of the currents shown on Fig.2d, the see-saw motion mostly impacts the polar motion through χ_2 . Due to the Chandler wobble resonance that dominates the polar motion^{16,17}, it is not possible to directly compare our model-derived estimates with polar motion observation. However, we can compute the excitation functions required to generate the observed polar motion during the strong see-saw of 2012-13.

Detection of 2012-13 event. The ocean is only one of the contributors to intraseasonal polar motion excitation - the atmosphere and the hydrology being the other sources¹⁸. An oceanic signal can only be separated from the climate noise if it is sensibly larger in the excitation than the non-oceanic contributions, or if we can correct the observed excitation with such precision that the residuals are notably smaller than the oceanic contribution. When dealing with intraseasonal excitation, the standard deviation, estimated over the last 10 years, is at the level of ~16 milliarcseconds (mas), to be compared with the 40 mas of the MJO-induced ocean signature, which makes it necessary to subtract the non-oceanic signal. The raw observed excitation during 2012-13 is plotted in Fig.4a, together with the residuals when the non-oceanic signals are subtracted. We observe a strong oceanic signal in early 2013. The MC-EXP captures about half of this signal, but the agreement in amplitude and phase between the residual excitation and the ocean excitation demonstrates that the small region of the Maritime Continent is indeed able to excite the Earth wobble to a detectable level during the strong MJO events.

Summary

The MJO winds, acting over ~4% of the Earth's surface, induce a global-scale ocean mass redistribution, which in turn affects the Earth rotation. This entire phenomenon is schematically illustrated in Fig.4b. The strong boreal winter MJO winds over the Maritime Continent elicit an intraseasonal large-scale barotropic response from the Indian and the Pacific Ocean whose extent, unlike previously known oceanic manifestations of the MJO, is not only limited to the tropics but also reaches the extratropics. The winds induce a barotropic circulation around the Australian continent and its periodic reversal at intraseasonal timescales is manifested as a see-saw in the oceanic mass within the Indo-Pacific basin. The large-scale oceanic mass redistribution in the Indo-Pacific basin, accompanied by large-scale to-and-fro transports in the two basins associated with this see-saw, benefits from a favourable geometry to excite polar motions, allowing the strong 2013 MJO event to be the first climate mode signature detected in the polar motion signal through the ocean.

The magnitude of the see-saw reported here implies that the intraseasonal barotropic variability of the ocean needs to be carefully considered when interpreting the mass budget of the various ocean basins. As the MJOs are intensifying and getting erratic with each passing year^{24,25}, detectable MJO signatures in the polar motion are expected to be more frequent in coming years.

Declarations

Acknowledgments: M.A is grateful to Mercator Ocean International for the academic visit. The authors are grateful to INCOIS and the Ministry of Earth Sciences (MoES) for providing facilities. This work is supported by INCOIS, MOES and by the project “Barotropic Influence on Global Ocean (BINGO); grant no 41-DS-GMMC-BINGO-CNRS195918”. The lead author is grateful to Council of Scientific and Industrial Research (CSIR) for providing Research Fellowship grant.

Author Contributions: A.P, F.D, B.R and S.S.C.S conceived the idea. M.A carried out the NEMO runs aided by B.R, R.B and F.D. P.V.S had carried out similar model experiments, supported by M.A and B.R, using coarser MOM5.0 in her project dissertation with A.P. B.R. processed the BPR data. A.P, F.D, B.R, M.A and R.B analysed the results. A.P., F.D and ODV wrote the manuscript and others corrected it. V.B provided bottom pressure data located at 37.283°W, 32.2548°N. All authors contributed to the material of the paper through multiple discussions. Authors declare no competing interests.

Data and materials availability: BPR data were downloaded from NDBC (<http://www.ndbc.noaa.gov/dart.shtml>), INCOIS/NIOT (<https://www.incois.gov.in>), ROSAME (<http://www.legos.obs-mip.fr/observations/rosame>), SAMOC(https://www.aoml.noaa.gov/phod/SAMOC_international), ABPR (<http://psc.apl.washington.edu/northpole/Data.html>) and BGEP (<https://www.whoi.edu/page.do?pid=66559>). BPR data located at 37.283°W, 32.2548°N have been obtained in the framework of EMSO-Azores observatory and can be obtained on request. National center for Medium Range Weather Forecasting (NCMRWF) fluxes are available from the Indian National Center for Ocean Information Services (INCOIS) on request. Real-time Multivariate MJO index (RMM) is available at <http://www.bom.gov.au/bmrc/clfor/cfstaff/matw/maproom/RMM/>. The Earth System Modelling Group of GeoForschungsZentrum Potsdam (ESMGFZ) data are available from <http://rz-vm115.gfz-potsdam.de:8080/repository>. International Earth Rotation and Reference Systems Service (IERS) polar motion excitations are downloaded from <https://hpiers.obspm.fr/eop-pc/analysis/excitactive.html>. International Nusantara Stratification And Transport (INSTANT) data are available from <http://www.marine.csiro.au/~cow074/index.htm>.

References

1. Madden, R. A. & Julian, P. R. Detection of a 40–50 Day Oscillation in the Zonal Wind in the Tropical Pacific. *J. Atmos. Sci.* **28**, 702–708 (1971).
2. Madden, R. A. & Julian, P. R. Description of Global-Scale Circulation Cells in the Tropics with a 40–50 Day Period. *J. Atmos. Sci.* **29**, 1109–1123 (1972).

3. Rohith, B. *et al.* Basin-wide sea level coherency in the tropical Indian Ocean driven by Madden–Julian Oscillation. *Nat. Commun.* **10**, 1257 (2019).
4. Zhang, C. Madden-Julian Oscillation. *Rev. Geophys.* **43**, RG2003 (2005)
5. Oliver, E. C. J. & Thompson, K. R. Madden-Julian Oscillation and sea level: Local and remote forcing. *J. Geophys. Res.* **115**, C01003 (2010).
6. Gross, R. S. Atmospheric and oceanic excitation of the Earth's wobbles during 1980–2000. *J. Geophys. Res.* **108**, 2370 (2003).
7. Gross, R. S., Fukumori, I., Menemenlis, D. & Gegout, P. Atmospheric and oceanic excitation of length-of-day variations during 1980-2000. *J. Geophys. Res. Solid Earth* **109**, B01406 (2004).
8. Lambeck, K. *The Earth's variable rotation*. Cambridge University Press, Cambridge, UK, 449 (1980).
9. Gross, R. S. Earth rotation variations-Long period, in Physical Geodesy, *Treatise on Geophysics*, T. A. Herring, Ed. Elsevier, Amsterdam, **11**, 239-294 (2007).
10. Barnes, R. T. H., Hide, R., White, A. A. & Wilson, C. A. Atmospheric angular momentum fluctuations, length-of-day changes and polar motion. *Proc. R. Soc. London. A. Math. Phys. Sci.* **387**, 31–73 (1983).
11. Madec, G. & the NEMO Team. NEMO ocean engine - version 3.6. *Note du Pôle modélisation*, Inst. Pierre-Simon Laplace, **27** (2014).
12. Wheeler, M. C. & Hendon,H. H. An All-Season Real-Time Multivariate MJO Index: Development of an Index for Monitoring and Prediction. *Mon. Weather Rev.* **132**, 1917-1932 (2004).
13. Cheng, X., Li, L., Du, Y., Wang, J. & Huang, R.-X. Mass-induced sea level change in the northwestern North Pacific and its contribution to total sea level change, *Geophys. Res. Lett.*, **40**, 3975-3980 (2013).
14. Fukumori, I., Wang, O., Llovel,W., Fenty,I. & Forget,G., A near-uniform fluctuation of ocean bottom pressure and sea level across the deep ocean basins of the Arctic Ocean and the Nordic Seas. *Prog. Oceanogr.* **134**, 152-172 (2015).
15. McCreary, J. P. *et al.* Interactions between the Indonesian Throughflow and circulations in the Indian and Pacific Oceans. *Prog. Oceanogr.* **75**, 70-114 (2007).
16. Chandler, S.C., On the variation of latitude, *I. Astron. J.* **11**, 59-61 (1981).
17. Gross, R. S., The excitation of the Chandler wobble, *Geophys. Res. Lett.*, **27**, 2329-2332 (2000).
18. Dehant, V., Viron, O. de & Barriot, J.-P. Geophysical excitation of the Earth orientation parameters EOP and its contribution to GGOS. *J. Geodyn.* **40**, 394-399 (2005).
19. Dill, R., Dobslaw, H. & Thomas, M. Improved 90-day Earth orientation predictions from angular momentum forecasts of atmosphere, ocean, and terrestrial hydrosphere. *J. Geod.* **93**, 287-295 (2019).
20. Dobslaw, H., Dill, R., Grötzsch, A., Brzeziński, A. & Thomas, M. Seasonal polar motion excitation from numerical models of atmosphere, ocean, and continental hydrosphere. *J. Geophys. Res.* **115**, B10406 (2010).

21. Dobslaw, H. & Dill, R. Predicting Earth orientation changes from global forecasts of atmosphere-hydrosphere dynamics. *Adv. Sp. Res.* **61**, 1047-1054 (2018).
22. Yu, N., Li, J., Ray, J. & Chen, W. Improved geophysical excitation of length-of-day constrained by Earth orientation parameters and satellite gravimetry products. *Geophys. J. Int.* **214**, 1633-1651 (2018).
23. Luo, J., Chen, W., Ray, J. & Li, J. Excitations of length-of-day seasonal variations: Analyses of harmonic and inharmonic fluctuations. *Geod. Geodyn.* **11**, 64-71 (2020).
24. Arnold, N. P., Branson, M., Kuang, Z., Randall, D. A. & Tziperman, E. MJO Intensification with Warming in the Superparameterized CESM. *J. Clim.* **28**, 2706-2724 (2015).
25. Haertel, P. Prospects for Erratic and Intensifying Madden-Julian Oscillations. *Climate* **8**, 24 (2020).
26. Marzocchi, A. *et al.* The North Atlantic subpolar circulation in an eddy-resolving global ocean model. *J. Mar. Syst.* **142**, 126 -143 (2015).
27. Smith, G. C. *et al.* Impact of Coupling with an Ice–Ocean Model on Global Medium-Range NWP Forecast Skill. *Mon. Weather Rev.* **146**, 1157-1180 (2018).
28. Rousset, C. *et al.* The Louvain-La-Neuve sea ice model LIM3.6: global and regional capabilities. *Geosci. Model Dev.* **8**, 2991-3005 (2015).
29. Lellouche, J.-M. *et al.* Recent updates to the Copernicus Marine Service global ocean monitoring and forecasting real-time 1/12° high-resolution system. *Ocean Sci.* **14**, 1093-1126 (2018).
30. Rieck, J. K., Böning, C. W., Greatbatch, R. J. & Scheinert, M. Seasonal variability of eddy kinetic energy in a global high-resolution ocean model. *Geophys. Res. Lett.* **42**, 9379-9386 (2015).
31. Gasparin, F. *et al.* A large-scale view of oceanic variability from 2007 to 2015 in the global high resolution monitoring and forecasting system at Mercator Océan. *J. Mar. Syst.* **187**, 260-276 (2018).
32. Adcroft, A., Hill, C. & Marshall, J. Representation of Topography by Shaved Cells in a Height Coordinate Ocean Model. *Mon. Weather Rev.* **125**, 2293-2315 (1997).
33. Bernard, B. *et al.* Impact of partial steps and momentum advection schemes in a global ocean circulation model at eddy-permitting resolution. *Ocean Dyn.* **56**, 543-567 (2006).
34. Shchepetkin, A. F., McWilliams, J. C., The regional oceanic modeling system (ROMS): a split-explicit, free-surface, topography-following-coordinate oceanic model. *Ocean Model.* **9**, 347-404 (2005).
35. Shchepetkin, A. F., McWilliams, J. C., Handbook of Numerical Analysis, : *Computational Methods for the Ocean and the Atmosphere*, P. G. Ciarlet, editor, R. Temam and J. Tribbia, guest eds., Elsevier Science, **14**, 121-183(2008).
36. Cravatte, S., Madec, G., Izumo, T., Menkes, C. & Bozec, A. Progress in the 3-D circulation of the eastern equatorial Pacific in a climate ocean model. *Ocean Model.* **17**, 28-48 (2007).
37. Lévy, M., Estublier, A. & Madec, G. Choice of an advection scheme for biogeochemical models. *Res. Lett.* **28**, 3725-3728 (2001).
38. Rodi, W. Examples of calculation methods for flow and mixing in stratified fluids. *J. Geophys. Res.* **92**, 5305 (1987).

39. Umlauf, L. & Burchard, H. A generic length-scale equation for geophysical turbulence models. *J. Mar. Res.* **61**, 235-265 (2003).
40. Reffray, G., Bourdalle-Badie, R. & Calone, C. Modelling turbulent vertical mixing sensitivity using a 1-D version of NEMO. *Geosci. Model Dev.* **8**, 69-86 (2015).
41. Ponte, R. M. Understanding the relation between wind- and pressure-driven sea level variability. *J. Geophys. Res.* **99**, 8033 (1994).
42. Dai, A., Qian, T., Trenberth, K. E. & Milliman, J. D. Changes in Continental Freshwater Discharge from 1948 to 2004. *J. Clim.* **22**, 2773-2792 (2009).
43. Amante, C. & W, E. B. ETOPO1 1 Arc-Minute Global Relief Model: Procedures, Data Sources and Analysis. NOAA Technical Memorandum *NESDIS NGDC-24*. Vasa. 19 (2009).
44. Becker, J. J. et al. Global Bathymetry and Elevation Data at 30 Arc Seconds Resolution: SRTM30_PLUS. *Mar. Geod.* **32**, 355-371 (2009).
45. Duchon, C. E. Lanczos Filtering in One and Two Dimensions. *J. Appl. Meteorol.* **18**, 1016-1022 (1979).
46. Dee, D. P. et al. The ERA-Interim reanalysis: configuration and performance of the data assimilation system. *Q. J. R. Meteorol. Soc.* **137**, 553-597 (2011).
47. Prasad, V. S. et al. Improvements in medium range weather forecasting system of India. *J. Earth Syst. Sci.* **123**, 247-258 (2014).
48. Locarnini, R. A. et al. S.Levitus, Ed.;A. Mishonov, Technical Ed, World Ocean Atlas 2013 Volume 1: Temperature . *NOAA Atlas NESDIS*. **73**,40 (2013).
49. Zweng, M. M. et al. S.Levitus, Ed.;A. Mishonov, Technical Ed, World Ocean Atlas 2013, Volume 2: Salinity, *NOAA Atlas NESDIS*. **74**, 39 (2013).
50. Large, W. G. & Yeager, S. G. The global climatology of an interannually varying air-sea flux data set. *Clim. Dyn.* **33**, 341-364 (2009).
51. Murray, M. T. A general method for the analysis of hourly heights of the tide. *Int. Hydrogr. Rev.* **41**, 91-101 (1964).
52. Chen, J.-L., Wilson, C. R., Hu, X.-G., Zhou, Y.-H. & Tapley, B. D. Oceanic effects on polar motion determined from an ocean model and satellite altimetry: 1993-2001. *J. Geophys. Res. Solid Earth.* **109**, B02411(2004).

Figures

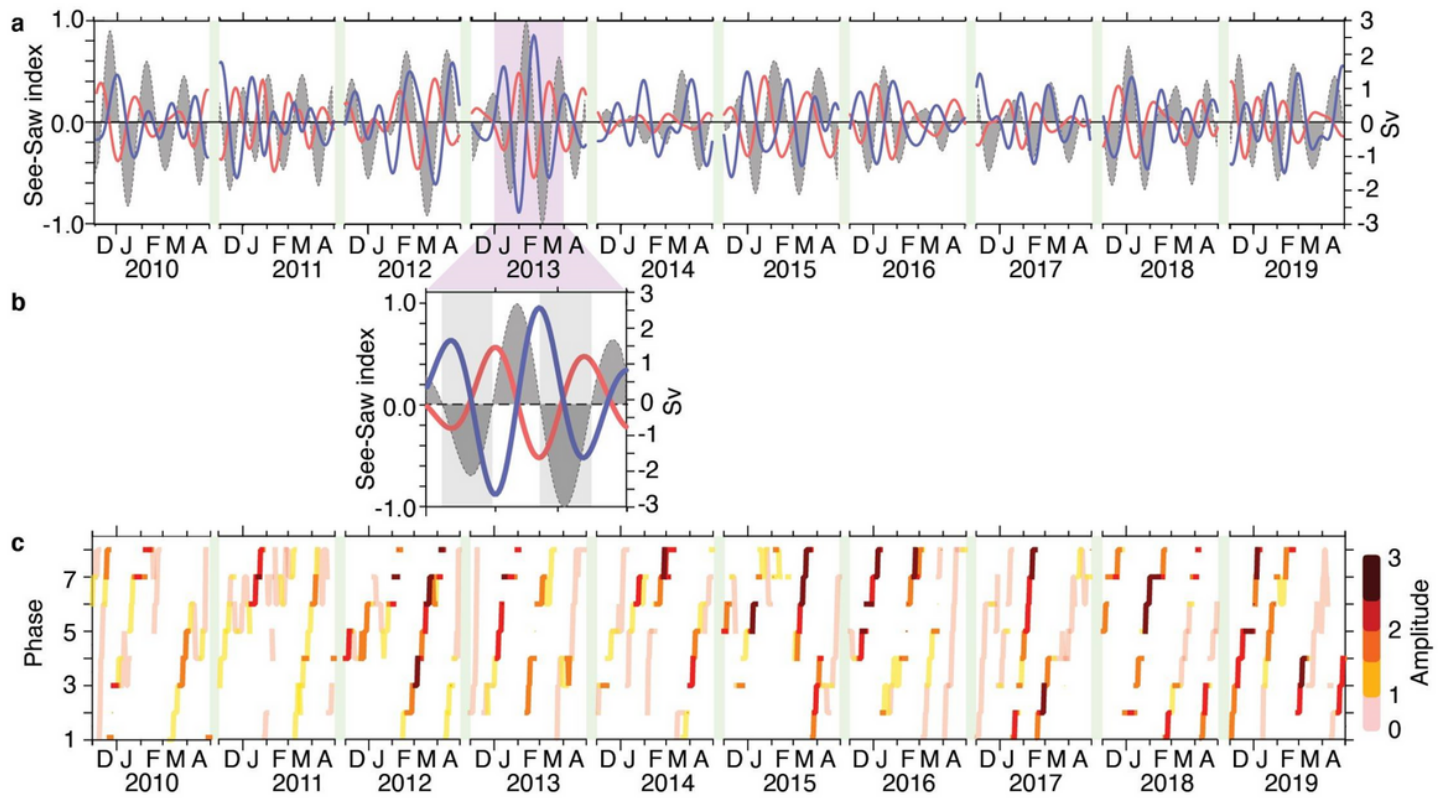


Figure 1

Transports in the Indo-Pacific basin and MJO index time-series. (a) Time series of the See-saw Index (shaded grey) and the net intraseasonal flux (in Sv) in the Indian (red line) and the Pacific (blue line) basin during each December-April of 2009-2019 estimated from the control run. (b) Inset of (a) for one strong see-saw event in early 2013. (c) Amplitude and phase of MJO index12 during 2009-2019. MJO is over the Maritime Continent when it is in between phases 3-6.

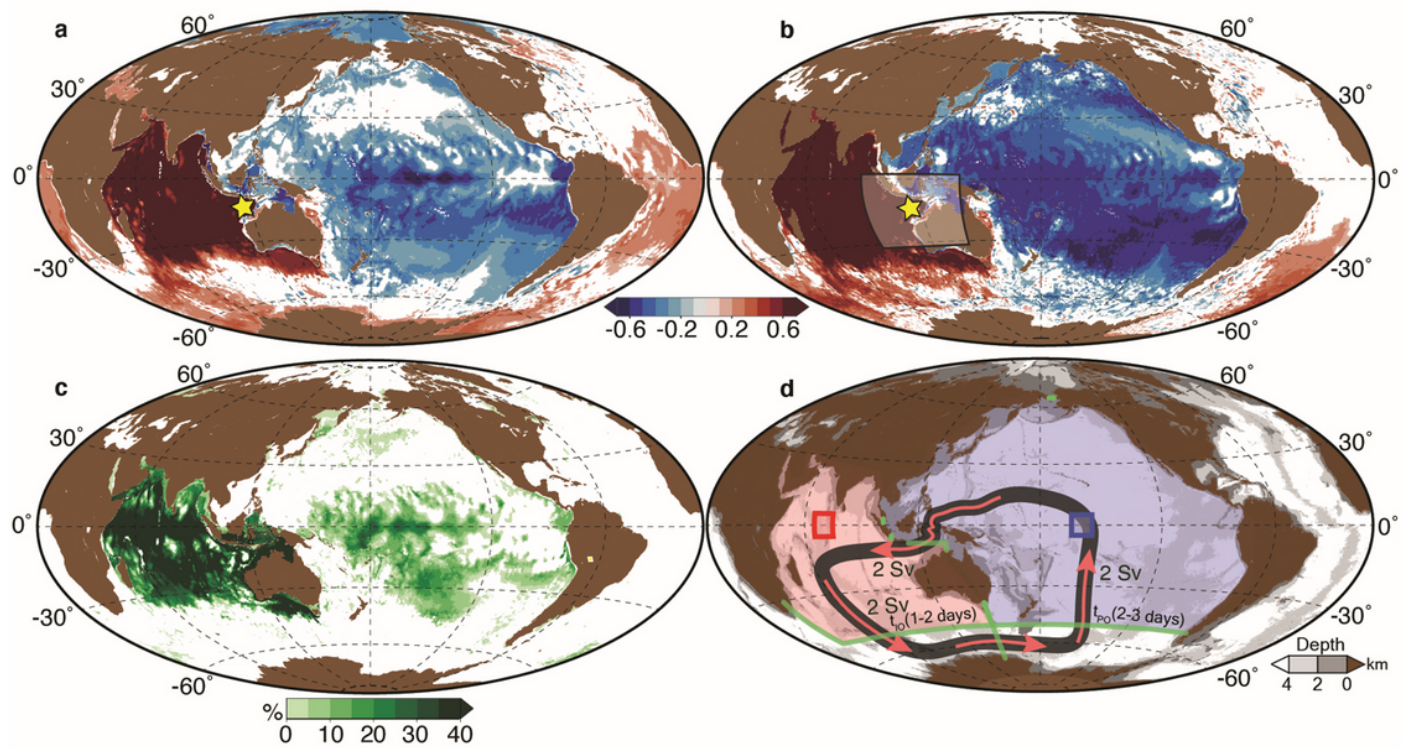


Figure 2

See-saw pattern and associated circulation. Plot of correlation ($>90\%$ significance) of intraseasonal EWDA over the Maritime Continent at 117.94°E , 15.02°S (yellow star) with respect to intraseasonal EWDA at all grid locations derived from (a) control run and (b) MC-EXP. (c) Percentage of intraseasonal EWDA variance in the control run explained by MC-EXP. The black box in (b) represents the extent of wind forcing in MC-EXP. (d) Schematic illustration of the intraseasonal barotropic circulation during a positive cycle of a see-saw event. The red (blue) tinge in the Indian (Pacific) Ocean represents a basin-wide rise (fall) in intraseasonal EWDA. The green lines define the boundaries of the Indian and Pacific basins. Mean intraseasonal EWDA difference over the red box ($65^{\circ}\text{E}:75^{\circ}\text{E}$, $5^{\circ}\text{S}:5^{\circ}\text{N}$) and the blue box ($155^{\circ}\text{W}:165^{\circ}\text{W}$, $5^{\circ}\text{S}:5^{\circ}\text{N}$) is used to define the see-saw index. t_{IO} and t_{PO} represent the delay in the intraseasonal transport with respect to the intraseasonal transport across ITF. Grey shades represent the bathymetry. Note: The designations employed and the presentation of the material on this map do not imply the expression of any opinion whatsoever on the part of Research Square concerning the legal status of any country, territory, city or area or of its authorities, or concerning the delimitation of its frontiers or boundaries. This map has been provided by the authors.

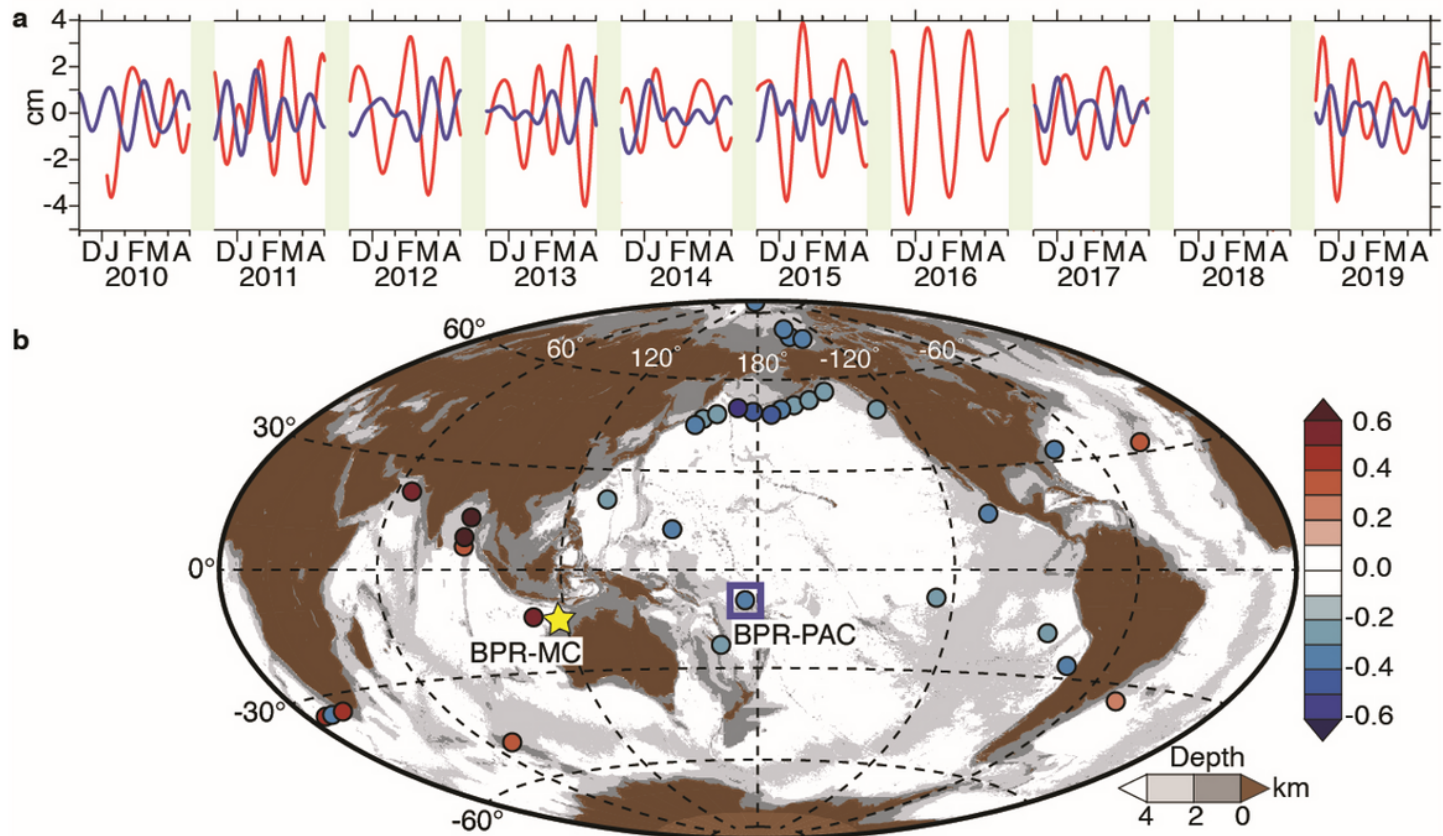


Figure 3

See-saw in the bottom pressure recorders. (a) Plot of intraseasonal EWDA at BPR-MC (solid red; 117.94°E, 15.02°S, 5664 m) and BPR-PAC (solid blue; 176.32°E, 9.517°S, 4921 m) during each December-April from 2009-2019. (b) Correlation (>90% significance) of intraseasonal EWDA from BPRs across the globe with respect to the intraseasonal EWDA at BPR-MC (yellow star). All other BPRs are marked as solid circles. Blue square box is used to mark BPR-PAC (blue box). The background colour shades represent the bathymetry. Number of BPRs analyzed in the Indian Ocean, Pacific Ocean, Atlantic Ocean and Arctic Ocean are 8, 45, 23 and 6 respectively. Note: The designations employed and the presentation of the material on this map do not imply the expression of any opinion whatsoever on the part of Research Square concerning the legal status of any country, territory, city or area or of its authorities, or concerning the delimitation of its frontiers or boundaries. This map has been provided by the authors.

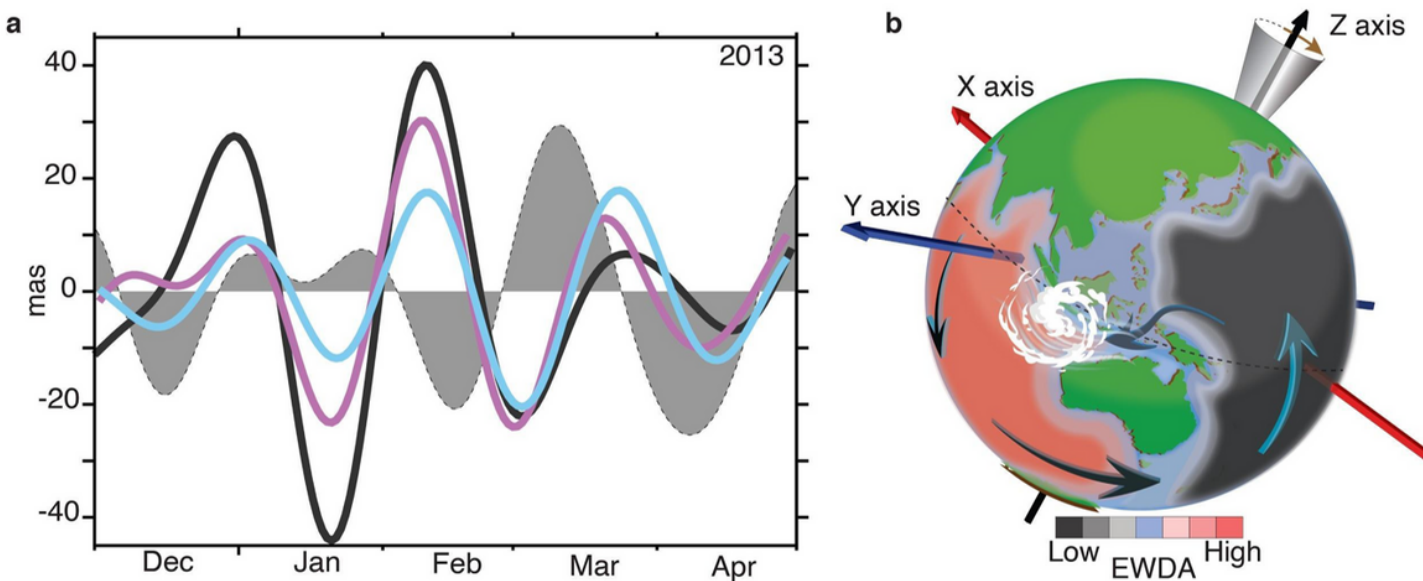


Figure 4

Ocean signature in polar motion (a) The plot of the time evolution of intraseasonal χ^2 from International Earth Rotation and Reference Systems Service (IERS) observations (grey shaded), residual of IERS observation after removing atmospheric and hydrological angular momentum from ESMGFZ19-23(black), χ^2 from control run (violet) and MC-EXP (cyan) during 2012-2013 boreal winter. (b) Schematic illustration of a positive cycle of the see-saw in the oceanic mass in the Indo-Pacific basin due to cyclonic boreal winter MJO winds over the Maritime Continent and its subsequent manifestation in the wobbling of the Earth at intraseasonal timescales. The green color represents landmasses. The color bar signifies intraseasonal EWDA. The white color over the Maritime Continent depicts a generic cyclonic wind pattern due to MJO. The anti-clockwise barotropic circulation around the Australian continent is denoted by the curly cyan arrows. The three axes of the solid Earth are represented by the red (x-axis), blue (y-axis) and black (z-axis) arrows. The wobbling of the z-axis is represented by the brown arrow. The black dashed line represents the Equator. The wind pattern and the arrows reverse direction during the negative cycle of the see-saw. Note: The designations employed and the presentation of the material on this map do not imply the expression of any opinion whatsoever on the part of Research Square concerning the legal status of any country, territory, city or area or of its authorities, or concerning the delimitation of its frontiers or boundaries. This map has been provided by the authors.

Supplementary Files

This is a list of supplementary files associated with this preprint. Click to download.

- [Supplementary.docx](#)